DESIGN OF COLD-FORMED HIGH STRENGTH STEEL RECTANGULAR HOLLOW SECTION T-JOINTS UNDER POST-FIRE CONDITIONS

Madhup Pandey[1,*] and Ben Young[2]

[1]*Department of Civil Engineering, University of Nottingham, Nottingham, United Kingdom.*
[2]*Department of Civil and Environmental Engineering, The Hong Kong Polytechnic University, Hong Kong, China.*

Abstract

A comprehensive numerical investigation looking into the static post-fire behaviour of cold-formed high strength steel (CFHSS) T-joints is presented in this paper. The braces and chords of T-joints were made of square and rectangular hollow section (SHS and RHS) members. The steel grade of SHS and RHS members was S960 with nominal 0.2% proof stress of 960 MPa. The static strengths of SHS and RHS T-joints were investigated corresponding to 4 post-fire temperatures, including 300°C, 550°C, 750°C and 900°C. Pandey and Young [1] carried out tests to investigate the post-fire residual strengths of cold-formed S960 steel grade SHS and RHS T-joints. The test results were used to develop an accurate finite element (FE) model. Through the validated FE model, a comprehensive FE parametric study was performed in this investigation. The validity ranges of critical geometric parameters were extended beyond current limits mentioned in international codes and guides. The nominal resistances predicted from design equations given in EC3 [2] and CIDECT [3], using post-fire material properties, were compared with a total of 765 test and FE joint resistances, including 756 numerical data obtained in this study. Overall, test and FE SHS and RHS T-joint specimens were failed by chord face failure, chord side wall failure and a combination of these two failure modes. Generally, the current design rules in EC3 [2] and CIDECT [3] are quite conservative and largely dispersed. As a result, accurate, less dispersed and reliable design equations are proposed in this study.

Keywords: Cold-formed steel; Design rules; FE analysis; High strength steel; Post-fire; Tubular joints.

[*]Corresponding author. (e-mail: madhup.pandey@nottingham.ac.uk).

1. Introduction

Tubular members are commonly used in various structures subjected to different types of loading. High torsional strength, superior aesthetical appearance, ability to confine in-filled material are some of the key merits that lead to the widespread popularity of tubular members. In addition, welding operations become quite easier when braces and chords are made of square and rectangular hollow section (SHS and RHS). After the 9/11 incident, researchers across the world recognised the impact of fire on structures. Consequently, adequate resistance under fire has now become one of the critical structural design considerations. In addition to meeting adequate structural resistance at peak fire temperature, the performance of a structure after the fire also needs significant attention. After cooling down to room temperature, residual forces locked inside the fire exposed structural members. Compared to member stresses at peak fire temperature, the residual shrinkage stresses could be quite severe. Hence, it is imperative to carry out a post-fire investigation before a fire exposed structure is allowed for its reuse. In the last six decades, only a few investigations [4-6] were carried out on the post-fire behaviour of normal strength steel (in this study, refer to steels with steel grades less than or equal to S460) tubular joints, while the majority of investigations were focused on the behaviour of tubular joints at room temperature. The post-fire behaviour of circular hollow section (CHS) T-joints made of Q345B steel grade was investigated by Jin et al. [4]. It was concluded that the effect of preload had no remarkable influence on the residual bearing capacity of the T-joints. Experimental and numerical studies were carried out by Gao et al. [5] to investigate the cyclic performance of fire exposed CHS T-joints made of normal strength steel. The CHS T-joints were reinforced with doubler plates. The energy dissipation capacities of CHS T-joints were significantly reduced after fire exposures. The post-fire behaviour of concrete in-filled CHS T-joints was experimentally and numerically investigated by Gao et al. [6]. It was found that the residual capacities of fire exposed concrete in-filled CHS T-joints were less than the residual capacities of corresponding fire exposed hollow CHS T-joints.

With regard to the post-fire behaviour of high strength steel tubular joints, to the best of the authors' knowledge, no other study is available except the experimental investigation conducted by Pandey and Young [1] on cold-formed S900 and S960 steel grades T- and X-joints. A comprehensive numerical investigation and design of fire exposed cold-formed RHS (henceforth, RHS includes SHS) T-joints of S960 steel grade are presented in this paper. Using test results [1], an accurate finite element (FE) model was developed in this investigation. A thorough parametric study comprising 756 FE analyses was carried out with the help of the verified FE model. The nominal resistances predicted from design rules given in EC3 [2] and CIDECT [3], using post-fire material properties, were compared with the residual strengths ($N_{f,\psi}$) of test and FE T-joint specimens. Generally, the current design rules in these specifications [2,3] are quite conservative and largely dispersed for the range of fire exposed RHS T-joints investigated in this study. Therefore, using two design methods, accurate and reliable design equations are proposed in this study to predict the $N_{f,\psi}$ of cold-formed S960 steel grade RHS T-joints subjected to post-fire temperatures ranging from 300°C to 900°C. In this paper, high strength steel (HSS) refers to steels with steel grades higher than S460.

2. Summary of test program

The static behaviour of fire exposed cold-formed high strength steel (CFHSS) T- and X-joints was investigated by Pandey and Young [1]. Before conducting the static joint tests, the test specimens were subjected to a total of three fire exposures. The preselected peak temperatures (ψ) of these three fire exposures were 300°C, 550°C and 750°C, respectively. In total, 9 T-joints made of RHS braces and chords were fabricated. The nominal 0.2% proof stress of without fire exposed RHS members was 960 MPa. The braces and chords were welded using robotic metal active gas welding. The test specimens were equally grouped into 3 series for the 3 fire exposures (i.e. ψ_1=300°C, ψ_2=550°C and ψ_3=750°C). All 3 series of test specimens were exposed to fire inside a gas furnace, where the furnace temperature was increased in accordance with ISO-834 [7]. After attaining the preselected peak temperatures (ψ), the test specimens were allowed to naturally cool inside the furnace. Subsequently, at room temperature, T-joint test specimens were axially compressed via braces with chord ends supported on rollers through end bearing blocks. Fig. 1 presents various notations for RHS T-joint. The static behaviour of RHS T-joint primarily depends on few geometric ratios, including β (b_1/b_0), τ (t_1/t_0), 2γ (b_0/t_0) and h_0/t_0. The symbols b, h, t and R stand for cross-section width, depth, thickness and external corner radius of RHS member, respectively. The subscripts 0 and 1 represent chord and brace, respectively. In the experimental investigation [1], β varied from 0.41 to 1.0, τ varied from 0.98 to 1.02, 2γ varied from 30.6 to 35.3 and h_0/t_0 varied from 30.6 to 35.5.

The lengths of braces (L_1) were equal to two times the maximum of b_1 and h_1. On the other hand, the lengths of chords (L_0) were equal to h_1+3h_0+180. The test results were obtained in the form of $N_{f,\psi}$ vs u and $N_{f,\psi}$ vs v curves, where $N_{f,\psi}$, u and v respectively stand for residual load, chord face indentation and chord side wall deformation. The material properties of ISO-834 [7] fire exposed S900 and S960 steel grades tubular members were investigated by Pandey and Young [8] for post-fire temperatures ranging from 300°C to 900°C. The test specimens in the experimental program [1] were fabricated from tubular members that belonged to the same batch of tubes used in Pandey and Young [8]. It should be noted that the cold-formed S960 steel grade RHS T-joints [1] and tubular members [8] were simultaneously exposed to fire inside the gas furnace. In addition to the 3 fire exposures (ψ_1=300°C, ψ_2=550°C and ψ_3=750°C) used in the investigation of the post-fire behaviour of RHS T-joints [1], the material properties of RHS members belonging to the identical mill batch were also investigated at 900°C (i.e. ψ_4=900°C) in Pandey and Young [8]. The measured values of static yield strength of fire exposed tubular members ranged from 1088 to 1145 MPa for ψ_1=300°C, 894 to 1023 MPa for ψ_2=550°C, 653 to 781 MPa for ψ_3=750°C and 310 to 347 MPa for ψ_4=900°C [8]. The details of the heating and cooling processes can also be obtained from Refs [9,10].

3. Numerical investigation

3.1. Finite element (FE) model

3.1.1. Introduction

ABAQUS [11] was used to perform comprehensive FE analyses. As the induced strains in the FE model during the applied load were unidirectional, the isotropic strain hardening law was selected for the analysis. The yielding onsets of FE models in this study were based on the von-Mises yield theory. In the FE analyses, the growth of the time step was kept non-linear in order to reduce the overall computation time. Furthermore, the default Newton-Raphson method was used to find the roots of non-linear equilibrium equations. The material non-linearities were considered in the FE models by assigning the measured values of post-fire residual static stress-strain curves. On the other hand, the geometric non-linearities in FE models were considered by enabling the non-linear geometry parameter (*NLGEOM) in ABAQUS [11]. Furthermore, various parameters, including through-thickness division, contact interactions, mesh seed spacing, corner region extension and element types, were also studied and reported in the following sub-sections of this paper. Fig. 2 presents typical FE T-joint specimens modelled in this study. The labelling of parametric FE specimens was kept identical to the label system used in the test program [1].

3.1.2. Mesh seed spacing, element type and material properties

Except for the welds, all other parts of the FE models were developed using second-order hexahedral elements, particularly using the C3D20 elements. On the other hand, the second-order tetrahedral element, C3D10, was used to model the weld parts due to their complicated shapes. The use of solid elements helped in making realistic fusions between tubular and weld parts of the FE models. Convergence studies were conducted using different mesh sizes, and finally, chord and brace members were seeded at 4 mm and 7 mm intervals, respectively, along their corresponding longitudinal and transverse directions. In order to assure the smooth transfer of stresses from flange to web regions, the corner portions of RHS were split into ten elements. FE analyses were also conducted to examine the influence of divisions along the wall thickness (t) of RHS members. The results of these FE analyses demonstrated trivial influence of wall thickness divisions on the load-deformation curves of the investigated RHS T-joints. The use of the C3D20 element as well as the small thickness of test specimens [1] lead to such observations. It is worth noting that similar findings were also obtained in other studies [12-14]. Thus, for the validation of FE model, the wall thickness of tubular members was not divided. The measured post-fire static stress-strain curves of flat and corner portions of RHS members [8] were assigned to the FE models. The measured post-fire material properties of tubular members corresponding to different post-fire temperatures are shown in Table 1, where the Young's modulus, 0.2% proof stress, ultimate strength and fracture strain are denoted by E, $\sigma_{0.2}$, σ_u and ε_f, respectively. The material properties of flat and corner regions are symbolised using sub-scripts f and c, respectively. In addition, post-fire material properties are represented using symbol ψ as a sub-script. However, experimentally obtained material curves were transformed into true stress-strain curves prior to their inclusion in the FE models. In the FE models, the influence of cold-working was included by assigning wider corner regions. Various distances for corner extension were considered in the sensitivity analyses, and finally, the corner portions were extended by $2t$ into the neighbouring flat portions, which was in agreement with other studies conducted on CFHSS tubular members and joints [12,13,15-18].

3.1.3. Weld modelling and contact interactions

The welds were modelled in all FE specimens using the measured average weld sizes reported in Pandey and Young [1]. The fillet weld was modelled for FE specimens with β = 0.41, 0.42 and 0.57. However, when β = 1.0, groove and fillet welds (GW and FW) were respectively modelled along the length and width of the chords. The inclusions of weld geometries appreciably improved the overall accuracies of FE models. A total of two types of contact interactions was defined in the FE models. First, contact interaction between brace and chord members of the FE models. Second, contact interaction between chord members and bearing blocks. In addition, a tie constraint was also established between weld and tubular members of the FE models. Both contact interactions were established using the built-in surface-to-surface contact definition. The contact interaction between brace and chord members of FE models was kept frictionless, while a frictional penalty equal to 0.3 was imposed on the contact interaction between chord member and bearing blocks. Along the normal direction of these two contact interactions, a 'hard' contact pressure overclosure was used. In addition, finite sliding was permitted between the interaction surfaces. For contact interactions and tie constraint, the surfaces were connected to each other using the 'master-slave' algorithm technique.

3.1.4. Boundary conditions

In order to apply boundary conditions, three reference points were created in each T-joint FE model, including one top reference point (TRP) and two bottom reference points (BRP-1 and BRP-2), as shown in Fig. 2. The TRP replicated the fixed boundary condition of the top brace end, while

BRP-1 and BRP-2 replicated the boundary conditions of the roller positioned at each chord end. The TRP was created at the cross-section centre of the top brace end, while BRP-1 and BRP-2 were created at 20 mm below the centre of the bottom surfaces of bearing blocks, which was in accordance with the test setup [1]. The TRP, BRP-1 and BRP-2 were then coupled to their corresponding surfaces using the built-in kinematic coupling type. In order to exactly replicate the boundary conditions of the T-joint test setup, all degrees of freedom (DOF) of TRP were restrained. On the other hand, for BRP-1 and BRP-2, except for the translations along the vertical and longitudinal directions of the T-joint FE specimen as well as the rotation about the transverse direction of the chord member, all other DOF of BRP-1 and BRP-2 were also restrained. In addition, all DOF of other nodes of T-joint FE specimen were kept unrestrained for both rotation and translation. Using the displacement control method, equal compression loads were then applied at the BRP-1 and 2 of FE models.

3.1.5. Geometric imperfection in chord webs

Garifullin et al. [19] studied the influence of geometric imperfections on the behaviour of cold-formed steel hollow section T-joints. The deformation scale of the first buckling mode was ramped up to match the tolerance limits given in EN [20]. It was concluded that the influence of geometric imperfections on the static behaviour of hollow section T-joints was trivial. However, Pandey et al. [12] reported that the maximum measured values of cross-section width and depth of RHS members were on an average 2.9% more than their respective nominal dimensions. As tubular members used in the post-fire investigation of RHS T-joints [1] also belonged to the identical batch of tubes used in Pandey et al. [12,21], thus, it was necessary to model this geometric imperfection as an outward bulging 3-point convex arc, as shown in Fig. 3. As all failure modes in tests [21,22] and numerical investigations [12,13] were only governed by the deformation of chord members, therefore, Pandey et al. [12,13] numerically examined the influence of outward bulging of chord cross-section on the static behaviour of hollow section joints. Finally, it was concluded that the effect of convex bulging of chord cross-section was only significant for equal-width (i.e. β=1.0) RHS T-joints. As a result, in this investigation, geometric imperfections were introduced as a 3-point convex arc in the chord webs of equal-width RHS T-joint FE models.

3.2. Validation of FE model

All modelling approaches described in the preceding section of this paper were used in the validation of FE models. The validation was performed by comparing the residual strengths ($N_{f,\psi}$), load-deformation histories and failure modes of test [1] and FE specimens. The measured dimensions of tubular members and welds were used to develop all FE models. In addition, measured post-fire residual static material properties of tubular members were used in the validation process. Table 2 presents the overall summary of comparisons between residual strengths ($N_{f,\psi}$) of T-joint test specimens and corresponding values predicted from their FE models (N_{FE}). The mean (P_m) and coefficients of variation (COV) (V_p) of the comparison are 1.00 and 0.012, respectively. It is worth mentioning that both ultimate load and 3% deformation limit load were used to determine the $N_{f,\psi}$ of test and FE specimens, whichever occurred earlier in the $N_{f,\psi}$ vs u curve. In addition, load vs deformation curves were compared between typical test and FE specimens, as shown in Figs. 4 and 5. In Figs. 4 and 5, slight discrepancies between the initial stiffnesses of test specimens and corresponding FE predictions could be due to the presence of residual stresses, which were not included in the FE models developed in this study. The effect of residual stresses on 3% deformation and ultimate resistances of the investigated joints are trivial and can be safely ignored. In both tests [1] and numerical investigation, chord face indentation values were consistently measured at 10 mm distance from the brace face. Furthermore, Figs. 6 and 7 present comparisons of distinct failure modes between typical test and FE specimens. Thus, the verified FE model precisely replicated the overall static behaviour of CFHSS fire exposed RHS T-joints, as shown in Table 2 and Figs. 4-7.

3.3. Parametric study

3.3.1. Details of finite element models

In the parametric study, 4 fire exposures with peak temperatures (ψ) equal to 300°C, 550°C, 750°C and 900°C were investigated, which were consistent with the test programs [1,8]. In total, 756 FE analyses were performed in the parametric study, including 189 FE analyses corresponding to each fire exposure. The parametric FE specimens were designed such that ψ varied from 300°C to 900°C, β varied from 0.30 to 1.0, 2γ varied from 16.6 to 50, h_0/t_0 varied from 10 to 60, η varied from

0.3 to 1.2 and τ varied from 0.75 to 1.25. The parametric study used all FE modelling techniques described earlier in this paper. In the numerical investigation, the values of cross-section width and depth of braces and chords of parametric FE specimens varied from 30 mm to 600 mm, while the wall thickness of braces and chords varied from 2.25 mm to 12.5 mm. The external corner radii of braces and chords (R_1 and R_0) conformed to commercially produced HSS members [23]. In this study, R_1 and R_0 were kept as $2t$ for $t \leq 6$ mm, $2.5t$ for $6 < t \leq 10$ mm and $3t$ for $t > 10$ mm, which in turn also meet the limits detailed in EN [20]. The formulae used to determine the lengths of braces and chords of parametric FE specimens were identical to those adopted in the test program [1], as detailed in Section 2 of this paper. For meshing along the longitudinal and transverse directions of tubular members, seedings were approximately spaced at the minimum of $b/30$ and $h/30$. Overall, the adopted mesh sizes of parametric FE specimens varied from 3 mm to 12 mm.

For RHS members with $t \leq 6$ mm, no divisions were made along the wall thickness of the parametric FE specimens. However, for RHS members with $t > 6$ mm, the wall thickness of parametric FE specimens was divided into two layers. With regard to the weld modelling, FW was modelled for FE specimens with $\beta \leq 0.80$. However, for FE specimens with $\beta > 0.80$, GW and FW were respectively modelled along the longitudinal and transverse directions of chords. Following the prequalified tubular joint details given in AWS D1.1M [24], the leg size of FW was designed as 1.5 times the minimum of t_1 and t_0. In addition, GW was designed in accordance with Figure 10.6 of prequalified tubular joint details given in AWS D1.1M [24], where the weld reinforcement (w_r) was taken as half of the minimum wall thickness of brace and chord member. The designs of both FW and GW were consistent with their corresponding designs adopted in the test program [1]. For different fire exposure series of the parametric study (i.e. ψ_1=300°C, ψ_2=550°C, ψ_3=750°C and ψ_4=900°C), the corresponding measured post-fire residual static material properties of flat and corner portions of RHS 120×120×4 [8] were assigned to the flat and corner portions of the FE specimens. Figs. 8(a) and 8(b) present the measured post-fire residual static stress-strain curves of the flat and corner portions of RHS 120×120×4 for different fire exposure series, respectively. Besides, the measured static weld material properties at room temperature [22] were retained as 100%, 85%, 57% and 48% for 300°C, 550°C, 750°C and 900°C post-fire temperatures, respectively. These retention percentages correspond to the average retention values of the ultimate stress of tubular members of different fire exposure series. Additionally, the flat parts of chord webs (i.e. h_0-2R_0) of all equal-width parametric T-joints of different fire exposure series were modelled as an outward bulging 3-point arc. The flat part of each chord web of equal-width RHS T-joint was outward bulged at its centre by 0.015b_0, as shown in Fig. 3.

3.3.2. Failure modes

Overall, three types of failure modes were identified in the experimental [1] and numerical investigations. First, failure of fire exposed RHS T-joint by chord flange yielding, which was termed as chord face failure and denoted by the letter 'F' in this study. Second, failure of fire exposed RHS T-joint due buckling of chord webs, which was termed as chord side wall failure and denoted by the letter 'S' in this study. Third, failure of fire exposed RHS T-joint due to the combination of chord face and chord side wall failures, which was named as combined failure and denoted by 'F+S' in this study. The test and parametric FE specimens were failed by the F mode, when the $N_{f,\psi}$ was determined using the 0.03b_0 limit. The applied loads of fire exposed RHS T-joints that failed by the F mode were monotonically increasing. The test and parametric FE specimens were failed by the F mode in this investigation, when $0.30 \leq \beta \leq 0.75$. On the other hand, test and parametric FE specimens were failed by the S mode in this investigation, when β=1.0. Moreover, the load-deformation curves exhibited clear ultimate load for parametric FE specimens that failed by the F+S mode. Additionally, evident deformations of chord flange, chord webs and chord corner regions were noticed in the parametric FE specimens that failed by the F+S mode. The specimens were failed by the F+S mode in this investigation when $0.80 \leq \beta \leq 0.90$. Moreover, none of the test and FE specimens were failed by the global buckling of braces. Figs. 9 to 11 present the variations of $N_{f,\psi}$ vs u curves of typical FE specimens that failed by F, F+S and S failure modes for all 4 post-fire temperatures, respectively.

4. EC3 [2] and CIDECT [3] design rules

Presently, design rules to predict the post-fire residual strengths of tubular joints are not given in any code and guideline. Therefore, in order to examine the suitability of EC3 [2] and CIDECT [3] design provisions for CFHSS fire exposed RHS T-joints, in this study, the nominal resistances from design equations given in EC3 [2] and CIDECT [3] ($N_{E,\psi}$ and $N_{C,\psi}$) were calculated using the measured post-fire residual static material properties reported in Pandey and Young [8]. The existing design rules given in EC3 [2] and CIDECT [3] are shown below:

Chord face failure ($\beta \leq 0.85$)

EC3 [2]:

$$N_{E,\psi} = C_f \left[k_n \frac{f_{y0,\psi} t_0^2}{(1-\beta)\sin\theta_1} \left(\frac{2\eta}{\sin\theta_1} + 4\sqrt{1-\beta} \right) / \gamma_{M5} \right] \tag{1}$$

CIDECT [3]:

$$N_{C,\psi} = C_f \left[Q_f \frac{f_{y0,\psi} t_0^2}{\sin\theta_1} \left(\frac{2\eta}{(1-\beta)\sin\theta_1} + \frac{4}{\sqrt{1-\beta}} \right) \right] \tag{2}$$

Chord side wall failure ($\beta = 1.0$)

EC3 [2]:

$$N_{E,\psi} = C_f \left[k_n \frac{f_{b,\psi} t_0}{\sin\theta_1} \left(\frac{2h_1}{\sin\theta_1} + 10t_0 \right) / \gamma_{M5} \right] \tag{3}$$

CIDECT [3]:

$$N_{C,\psi} = C_f \left[Q_f \frac{f_{k,\psi} t_0}{\sin\theta_1} \left(\frac{2h_1}{\sin\theta_1} + 10t_0 \right) \right] \tag{4}$$

The nominal resistances from design equations given in EC3 [2] were obtained using 0.2% proof stress and partial safety factor (γ_{M5}) equal to 1.0. In addition, a material factor (C_f) equal to 0.80 was adopted as per EC3 [25]. On the other hand, CIDECT [3] uses the minimum of 0.2% proof stress and 0.80 times the corresponding ultimate stress for joint resistance calculation. Moreover, design provisions given in CIDECT [3] recommend the use of C_f equal to 0.90 for tubular joints with steel grade exceeding S355. Referring to IIW [26], the value of partial safety factor (γ_M) for RHS T-joints failed by both chord face failure and chord side wall failure modes is equal to 1.0. Thus, nominal resistances from CIDECT [3] were calculated using γ_M equal to 1.0 for both chord face failure and chord side wall failure modes. In Eqs. (1) to (4), chord stress functions are denoted by k_n and Q_f, post-fire yield stress of chord member is denoted by $f_{y0,\psi}$, the parameter η is equal to h_1/b_0, post-fire chord side wall buckling stresses are denoted by $f_{b,\psi}$ and $f_{k,\psi}$, and the angle between brace and chord is denoted by θ_1 (in degrees).

In addition, a reliability analysis was performed as per AISI S100 [27]. In this study, a design equation was treated as reliable when the value of reliability index (β_0) was greater than or equal to 2.50. The values of various statistical parameters and load combinations used in the reliability index calculation are identical to those values adopted in Pandey et al. [12].

5. Comparisons of residual joint strengths with nominal resistances

For different observed failure modes, the overall summary of comparisons between $N_{f,\psi}$ and nominal resistances predicted from design equations given in EC3 [2] and CIDECT [3] are shown in Tables 3 to 5. In total, 765 data are presented in Tables 3 to 5, including 9 test data [1] and 756 parametric FE data generated in this study. The comparisons are also graphically shown in Figs. 12 to 14 for different failure modes. In Fig. 12, generally, test and parametric FE specimens with small values of β and η ratios and large values of 2γ ratio lie below the unit-slope line (i.e. y=x). For such FE specimens, the joint resistance corresponding to the $0.03b_0$ limit was not sufficient to cause the yielding of the chord flange. On the contrary, the yield line theory was used to derive the existing design equation for T-joint specimens that failed by the F mode [2,3]. Consequently, $N_{f,\psi}$ of test and parametric FE specimens became smaller than the corresponding nominal resistances predicted from design equations given in EC3 [2] and CIDECT [3]. As a result, such data fall below the line of unit slope. For those data which lie above the line of unit slope, on the other hand, indicate test and parametric FE specimens with medium to large values of β and η ratios and small values of 2γ ratio. The stress-strain behaviour of HSS material is quite different to that of mild steel [28-31], which could change the deformation extent of chord connecting faces. The data above the unit-slope line in Fig. 13 typically represent RHS T-joints with large values of β ratio and small values of 2γ and h_0/t_0 ratios. As the β ratio of the RHS T-joint failed by the F+S mode increased, the brace member gradually approached the chord corner regions. Consequently, $N_{f,\psi}$ of such joints increased because of the enhanced rigidity of corner regions. On the other hand, the corresponding increase in nominal resistances predicted from design equations given in EC3 [2] and CIDECT [3] was lower than the $N_{f,\psi}$ of FE T-joints. Subsequently, such data fall above the line of unit slope in Fig. 13. The comparison results of the test and parametric FE specimens that failed by the S mode is shown in Fig. 14. The existing design rules apparently provided very conservative predictions and were accompanied by very large values of COV. The EC3 [2] and CIDECT [3] design provisions for S failure mode considered chord webs as pin-ended columns, which resulted in very conservative predictions as h_0/t_0 ratio increased.

6. Proposed design rules

Using two design methods, named as proposal-1 and -2, design rules are proposed in this study for different failure modes of the investigated RHS T-joints. The design rules proposed in both design methods (i.e. proposal-1 and -2) are based on design equations proposed by Pandey et al. [12] for without fire exposed S960 steel grade RHS T-joints. In the first design method (i.e. proposal-1), the room temperature material properties used in the design equations proposed by Pandey et al. [12] are replaced with the corresponding post-fire residual material properties. In addition, a correction factor (ξ) based on post-fire peak temperature (ψ) is also applied on the proposed design rules under proposal-1. On the other hand, in the second design method (i.e. proposal-2), only a correction factor based on the post-fire peak temperature (ψ) is applied on the design rules proposed by Pandey et al. [12] using room temperature material properties. Therefore, design equations under proposal-1 can predict the $N_{f,\psi}$ of fire exposed RHS T-joints when post-fire residual material properties are available. However, design equations under proposal-2 can predict the $N_{f,\psi}$ only using the post-fire peak temperature (ψ). It should be noted that the design rules proposed in this study are valid for 300°C ≤ ψ ≤ 900°C. As welds were modelled in all parametric FE specimens, the influence of welds is implicitly included in the proposed design rules. In order to obtain design resistances (N_d), the proposed nominal resistances (N_{pn1} and N_{pn2}) in the following sub-sections of this paper shall be multiplied by their correspondingly recommended resistance factors (ϕ), i.e. $N_d = \phi$ (N_{pn1} or N_{pn2}).

6.1. RHS T-joints failed by F mode

<u>Proposal-1:</u>

Using post-fire material properties and post-fire peak temperature (ψ) correction factor:

$$N_{pn1} = \xi\left[f_{y0,\psi} t_0^2 \left(\frac{30\beta + 4.5\eta - 6.6}{0.5 + 0.03(2\gamma)} \right) \right] \tag{5}$$

where

$$\xi = \begin{bmatrix} 0.0002\psi + 0.85 & \text{for} & 300°\text{C} \le \psi \le 750°\text{C} \\ 0.0024\psi - 0.80 & \text{for} & 750°\text{C} < \psi \le 900°\text{C} \end{bmatrix} \tag{6}$$

<u>Proposal-2:</u>

Using room temperature material properties and post-fire peak temperature (ψ) correction factor:

$$N_{pn2} = (1.17 - 0.0008\psi)\left[f_{y0} t_0^2 \left(\frac{30\beta + 4.5\eta - 6.6}{0.5 + 0.03(2\gamma)} \right) \right] \tag{7}$$

The Eqs. (5) and (7) are valid for $0.30 \le \beta \le 0.75$, $16.6 \le 2\gamma \le 50$, $16.6 \le h_0/t_0 \le 50$, $0.3 \le \eta \le 1.2$ and $0.75 \le \tau \le 1.0$. Both Eqs. (5) and (7) must be multiplied by ϕ equal to 0.75 to obtain the corresponding design resistances (N_d). The comparisons of $N_{f,\psi}$ of test and FE specimens with nominal resistances predicted from design equations given in EC3 [2], CIDECT [3] as well as predictions from proposal-1 and -2 are graphically presented in Fig. 12. The comparison results are detailed in Table 3.

6.2. RHS T-joints failed by F+S mode

<u>Proposal-1:</u>

Using post-fire material properties and post-fire peak temperature (ψ) correction factor:

$$N_{pn1} = \xi\left[f_{y0,\psi} t_0^2 \left(\frac{55\beta + 4.5\eta - 33}{0.75 + 0.0075(2\gamma)} \right) \right] \tag{8}$$

where

$$\xi = \begin{bmatrix} 0.85 & \text{for} & 300°\text{C} \le \psi \le 750°\text{C} \\ 0.003\psi - 1.4 & \text{for} & 750°\text{C} < \psi \le 900°\text{C} \end{bmatrix} \tag{9}$$

<u>Proposal-2:</u>

Using room temperature material properties and post-fire peak temperature (ψ) correction factor:

$$N_{pn2} = \left(1.14 - 0.0008\psi\right)\left[f_{y0} t_0^2 \left(\frac{55\beta + 4.5\eta - 33}{0.75 + 0.0075\left(2\gamma\right)} \right) \right] \tag{10}$$

The Eqs. (8) and (10) are valid for $0.80 \leq \beta \leq 0.90$, $16.6 \leq 2\gamma \leq 50$, $16.6 \leq h_0/t_0 \leq 50$, $0.6 \leq \eta \leq 1.2$ and $0.75 \leq \tau \leq 1.0$. Both Eqs. (8) and (10) must be multiplied by ϕ equal to 0.70 to obtain the corresponding design resistances (N_d). The comparisons of $N_{f,\psi}$ of RHS T-joints with nominal resistances predicted from design equations given in EC3 [2], CIDECT [3] as well as predictions from proposal-1 and -2 are graphically presented in Fig. 13. The comparison results are detailed in Table 4.

6.3. RHS T-joints failed by S mode

Proposal-1:

Using post-fire material properties and post-fire peak temperature (ψ) correction factor:

$$N_{pn1} = \left(1.15 - 0.0006\psi\right)\left[\frac{f_{k,\psi}\left(2b_w t_0\right)}{\left(1.5\eta + 1\right)} \left(\frac{1.83 - 0.05\left(2\gamma\right) + 1.2\tau}{588\left(\frac{h_0}{t_0}\right)^{-2.17}} \right) \right] \tag{11}$$

Proposal-2:

Using room temperature material properties and post-fire peak temperature (ψ) correction factor:

$$N_{pn2} = \left(1.33 - 0.001\psi\right)\left[\frac{f_k\left(2b_w t_0\right)}{\left(1.5\eta + 1\right)} \left(\frac{1.83 - 0.05\left(2\gamma\right) + 1.2\tau}{588\left(\frac{h_0}{t_0}\right)^{-2.17}} \right) \right] \tag{12}$$

The Eqs. (11) and (12) are valid for $\beta = 1.0$, $16.6 \leq 2\gamma \leq 50$, $10 \leq h_0/t_0 \leq 60$, $0.6 \leq \eta \leq 1.2$ and $0.75 \leq \tau \leq 1.25$. The Eqs. (11) and (12) must be multiplied by ϕ equal to 0.75 and 0.70, respectively, to obtain the corresponding design resistances (N_d). The comparisons of $N_{f,\psi}$ of test and FE specimens with nominal resistances predicted from design equations given in EC3 [2], CIDECT [3] as well as predictions from proposal-1 and -2 are graphically presented in Fig. 14. The comparison results are detailed in Table 5. The buckling curve 'a' given in EC3 [32] is used to determine the $f_{k,\psi}$ and f_k in Eqs. (11) and (12). Moreover, the effective length of the flat portion of chord side wall is equal to $0.85\times(h_0\text{-}2R_0)$. The definition of the width of the chord web column (b_w) is identical to the value given in EC3 [2] and CIDECT [3].

It is important to note that for RHS T-joint specimens with $0.75 < \beta < 0.80$ and $0.90 < \beta < 1.0$, the nominal resistances under proposal-1 can be obtained by performing linear interpolation between Eqs. (5) and (8) as well as Eqs. (8) and (11), respectively. Similarly, under proposal-2, the nominal resistances of RHS T-joint specimens with $0.75 < \beta < 0.80$ and $0.90 < \beta < 1.0$ can be obtained by performing linear interpolation between Eqs. (7) and (10) as well as Eqs. (10) and (12), respectively.

7. Conclusions

This paper presents an extensive numerical investigation of the post-fire static behaviour of cold-formed S960 steel grade SHS and RHS T-joints under axial compression loads. The static behaviour of SHS and RHS T-joints was numerically investigated corresponding to 4 post-fire temperatures, including 300°C, 550°C, 750°C and 900°C. The measured post-fire residual static material properties of S960 steel grade tubular members [8] were used to perform the numerical investigation in this study. The validated finite element (FE) model precisely replicated the overall static behaviour of SHS and RHS T-joints for all post-fire temperatures. The weld parts were modelled in all parametric FE specimens, which in turn improved the overall accuracy of the numerical results. The investigated fire exposed SHS and RHS T-joints were failed by chord face failure (F), chord side wall failure (S), and a combination of these two failure modes, i.e. combined failure (F+S) mode. The residual strengths of SHS and RHS T-joints were compared with the nominal resistances predicted from design equations given in EC3 [2] and CIDECT [3] using the measured post-fire residual static material properties. Generally, it is shown that the current design provisions given in EC3 [2] and CIDECT [3] are quite conservative and largely dispersed for the range of fire exposed SHS and RHS T-joints investigated in this study with extended validity limits of critical geometric parameters. As a result, accurate, less dispersed and reliable design rules are proposed in this study to predict the nominal resistances of S960 steel grade SHS and RHS T-joints under post-fire temperatures ranging from 300°C to 900°C.

Acknowledgement

The work described in this paper was fully supported by a grant from the Research Grants Council of the Hong Kong Special Administrative Region, China (Project No. 17210218).

References

[1] Pandey M and Young B. Post-Fire Behaviour of Cold-Formed High Strength Steel Tubular T- and X-Joints, Journal of Constructional Steel Research 2021;186:106859.

[2] Eurocode 3 (EC3), Design of Steel Structures-Part 1-8: Design of Joints, EN 1993-1-8, European Committee for Standardization, CEN, Brussels, Belgium, 2005.

[3] Packer JA, Wardenier J, Zhao XL, Vegte GJ van der, Kurobane Y. Design guide for rectangular hollow section (RHS) joints under predominantly static loading. Comite´ International pour le Developpement et l'Etude de la Construction TuECbulaire (CIDECT), Design Guide No. 3, 2nd edn., LSS Verlag, Dortmund, Germany, 2009.

[4] Jin M, Zhao J, Chang J and Zhang D. Experimental and parametric study on the post-fire behavior of tubular T-joint. Journal of Constructional Steel Research, 70, 93-100. 2012.

[5] Gao F, Gua, XQ, Zhu HP and Xia Y. Hysteretic behaviour of tubular T-joints reinforced with doubler plates after fire exposure. Thin-Walled Structures, 92, 10-20, 2015.

[6] Gao F, Zhu H, Liang H and Tian Y. Post-fire residual strength of steel tubular T-joint with concrete-filled chord. Journal of Constructional Steel Research, 139, 327-338, 2017.

[7] ISO-834. Fire-resistance tests-Elements of Building Construction-Part 1-General requirements. ISO 834-1, International Organization of Standards, 1999.

[8] Pandey M and Young B. Post-fire Mechanical Response of High Strength Steels. Thin-Walled Structures, 164 (2021) 107606.

[9] Chen MT, Pandey M and Young B. Mechanical Properties of Cold-Formed Steel Semi-Oval Hollow Sections after Exposure to ISO-834 Fire, Thin-walled Structures, 2021;167:108202.

[10] Chen MT, Pandey M and Young B. Post-fire residual material properties of cold-formed steel elliptical hollow sections. Journal of Constructional Steel Research, 2021;183:106723.

[11] Abaqus/Standard. Version 6.17. USA: K. a. S. Hibbit; 2017.

[12] Pandey M, Chung KF and Young B. Design of cold-formed high strength steel tubular T-joints under compression loads. Thin-Walled Structures 2021;164:107573.

[13] Pandey M, Chung KF and Young B. Numerical investigation and design of fully chord supported tubular T-joints. Engineering Structures 2021;239:112063.

[14] Crockett P. Finite element analysis of welded tubular connections. PhD Thesis, University of Nottingham, 1994.

[15] Chen MT and Young B. Beam-column design of cold-formed steel semi-oval hollow non-slender sections. Thin-Walled Structures, 2021;162:107376.

[16] Chen MT and Young B. Numerical analysis and design of cold-formed steel elliptical hollow sections under combined compression and bending. Engineering Structures, 2021;241:112417.

[17] Ma JL, Chan TM and Young B. Design of cold-formed high strength steel tubular beams. Engineering Structures 2017; 151:432-443.

[18] Su A, Sun Y, Zhao O and Liang Y. Local buckling of S960 ultra-high strength steel welded I-sections subjected to combined compression and major-axis bending. Engineering Structures, 2021;248:113213.

[19] Garifullin M, Bronzova MK, Heinisuo M, Mela K and Pajunen S. Cold-formed RHS T joints with initial geometrical imperfections. Magazine of Civil Engineering 2018,82(6).

[20] prEN 10219-2. Cold formed welded structural hollow sections of non-alloy and fine grain steels-Part 2: Tolerances, dimensions and sectional properties. European Committee for Standardization (CEN), Brussels, Belgium; 2006.

[21] Pandey M and Young B. Tests of cold-formed high strength steel tubular T-joints. Thin-Walled Struct 2019;143:106200.

[22] Pandey M and Young B. Compression capacities of cold-formed high strength steel tubular T-

joints. J Constr Steel Res 2019;162:105650.
[23] SSAB. Strenx Tube 960 MH. Data Sheet 2043, Sweden, 2017.
[24] AWS D1.1/D1.1M, Structural Welding Code – Steel, American Welding Society (AWS), Miami, USA, 2020.
[25] Eurocode 3 (EC3), Design of steel structures. Part 1-12: Additional rules for the extension of EN 1993 up to steel grades S700, EN 1993-1-12, European Committee for Standardization, CEN, Brussels, Belgium, 2007.
[26] IIW Doc. XV-1402-12 and IIW Doc. XV-E-12-433. Static design procedure for welded hollow section joints – Recommendations. International Institute of Welding, Paris, France, 2012.
[27] AISI S100. North American Specification for the design of cold-formed steel structural members. American Iron and Steel Institute (AISI), Washington, D.C., USA, 2016.
[28] Pandey M and Young B. Ultimate Resistances of Member-Rotated Cold-Formed High Strength Steel Tubular T-Joints under Compression Loads, Engineering Structures 2021;244:112601.
[29] Pandey M and Young B. Effect of Member Orientation on the Static Strengths of Cold-Formed High Strength Steel Tubular X-Joints, Thin-walled Structures 2022;170:108501.
[30] Pandey M and Young B. Stress Concentration Factors of Cold-Formed High Strength Steel Tubular T-Joints, Thin-walled Structures 2021;166:107996.
[31] Pandey M and Young B. Experimental Investigation on Stress Concentration Factors of Cold-formed High Strength Steel Tubular X-Joints, Engineering Structures 2021;243:112408.
[32] Eurocode 3 (EC3), Design of Steel Structures–Part 1-1: General Rules and Rules for Buildings, EN 1993-1-1, European Committee for Standardization (CEN), Brussels, Belgium, 2005.

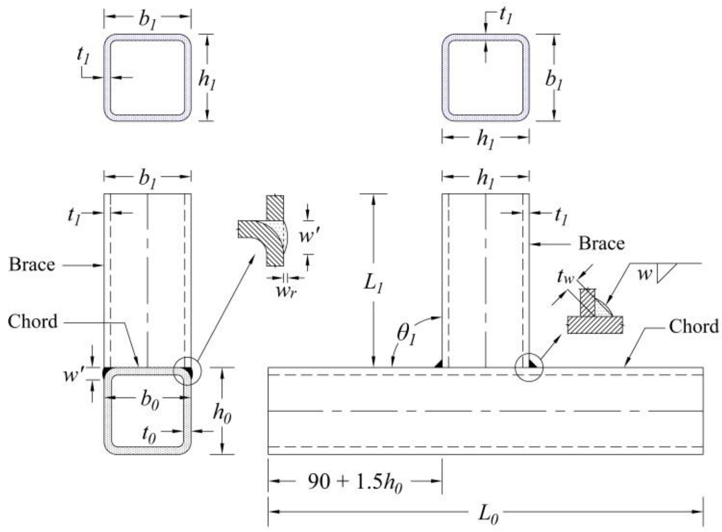

Fig. 1. Definitions of notations for RHS T-joint.

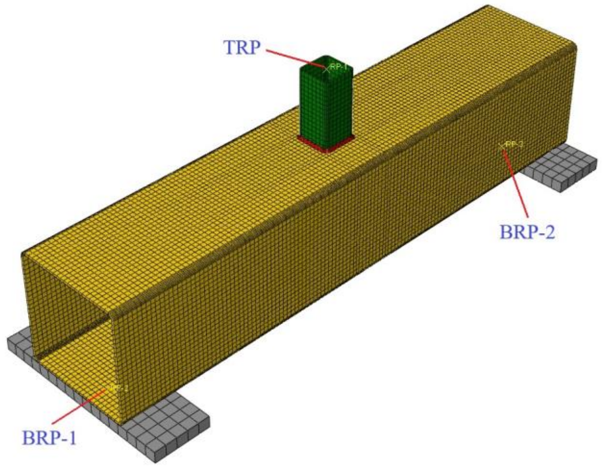

(a) Typical RHS T-joint FE model with β=0.30.

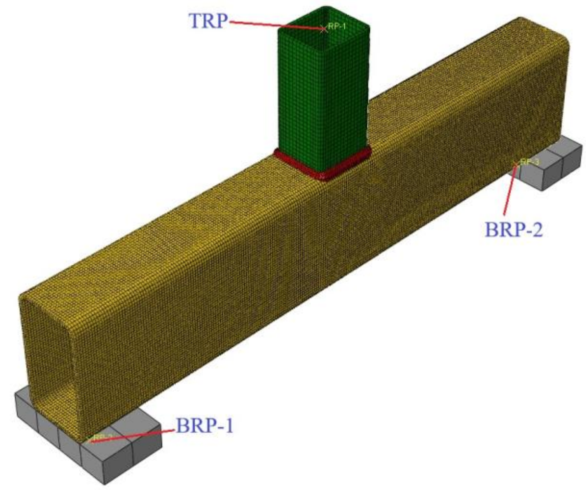

(b) Typical RHS T-joint FE model with β=0.80.

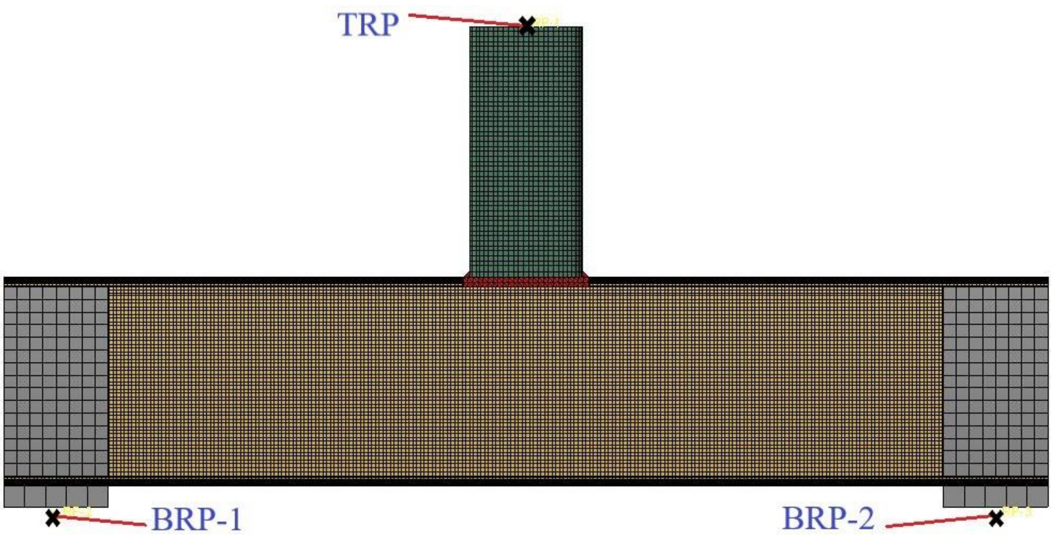

(c) Typical RHS T-joint FE model with β=1.0.

Fig. 2. Typical FE models of RHS T-joints.

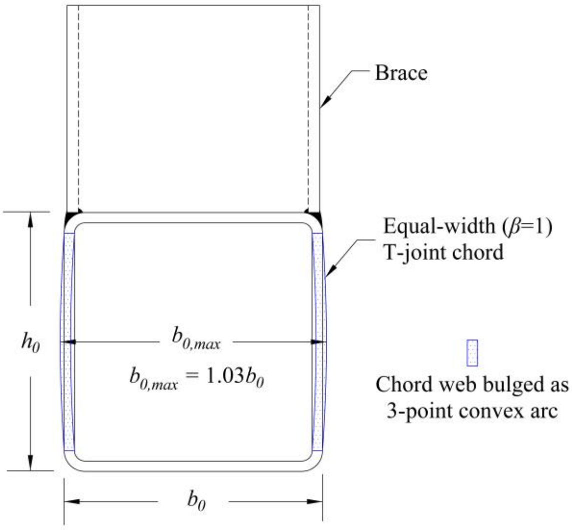

Fig. 3. Modelling of initial imperfection in chord webs of equal-width (β=1.0) RHS T-joints.

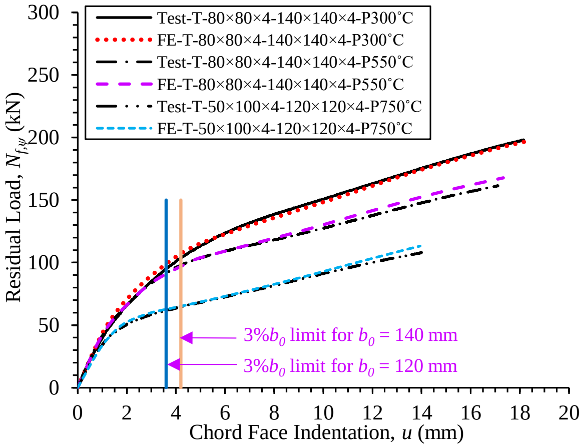

(a) Load vs chord face indentation curves.

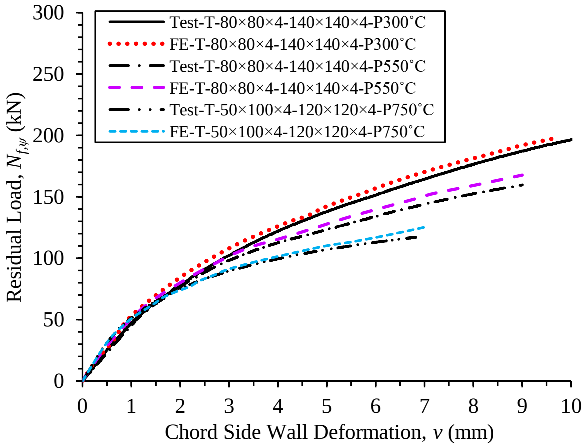

(b) Load vs chord side wall deformation curves.

Fig. 4. Test vs FE load-deformation curves for RHS T-joints failed by F mode.

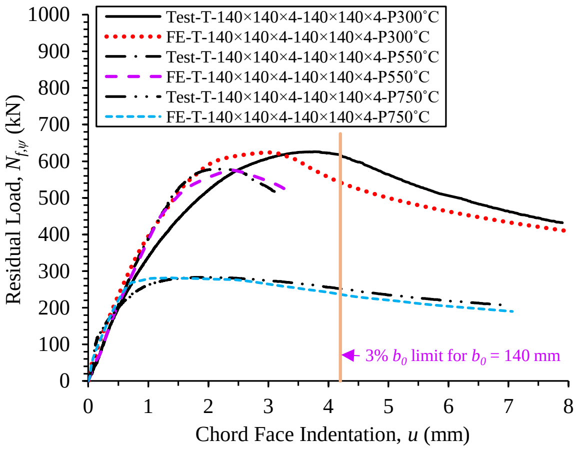

(a) Load vs chord face indentation curves.

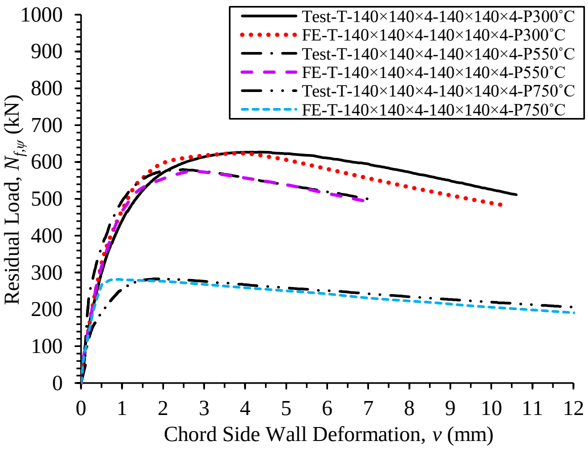

(b) Load vs chord side wall deformation curves.

Fig. 5. Test vs FE load-deformation curves for RHS T-joints failed by S mode.

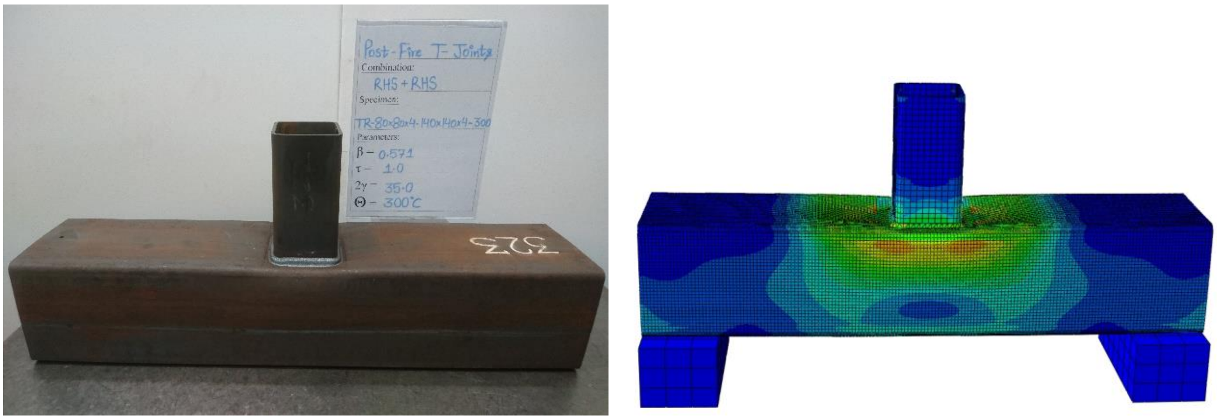

(a) Test vs FE comparison for RHS T-joint with ψ = 300°C and failed by F mode.

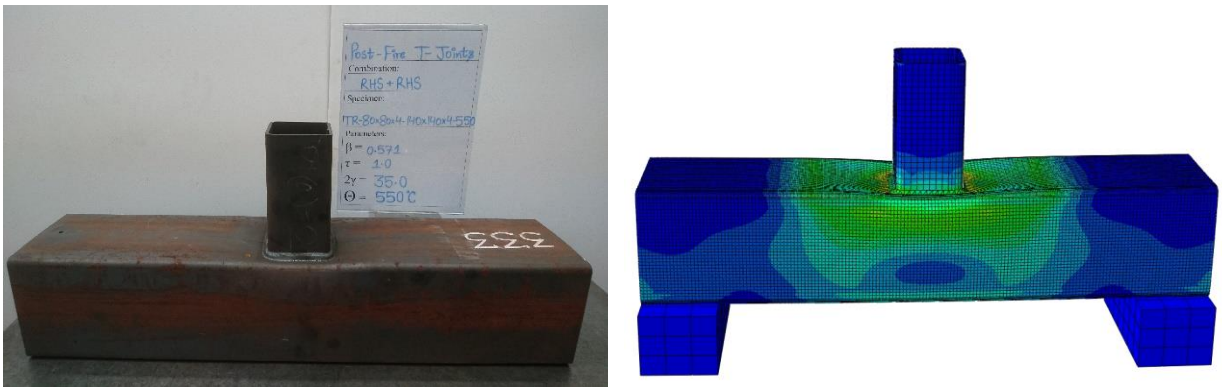

(b) Test vs FE comparison for RHS T-joint with ψ = 550°C and failed by F mode.

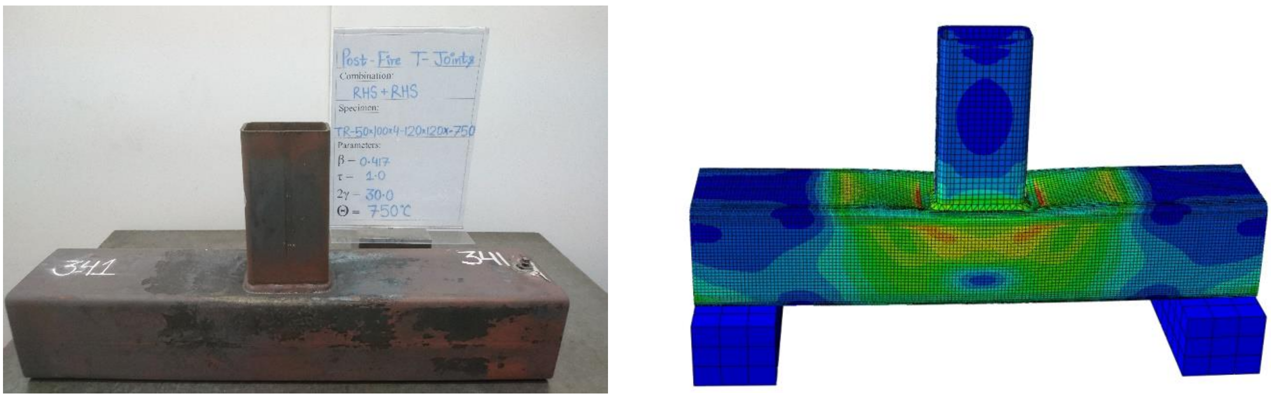

(c) Test vs FE comparison for RHS T-joint with ψ = 750°C and failed by F mode.

Fig. 6. Test vs FE comparisons for RHS T-joints failed by F mode.

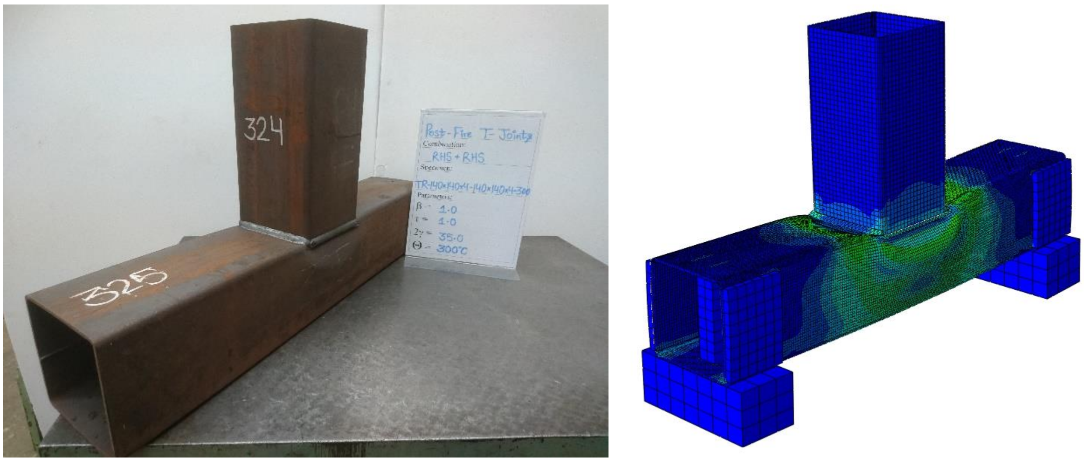

(a) Test vs FE comparison for RHS T-joint with ψ = 300°C and failed by S mode.

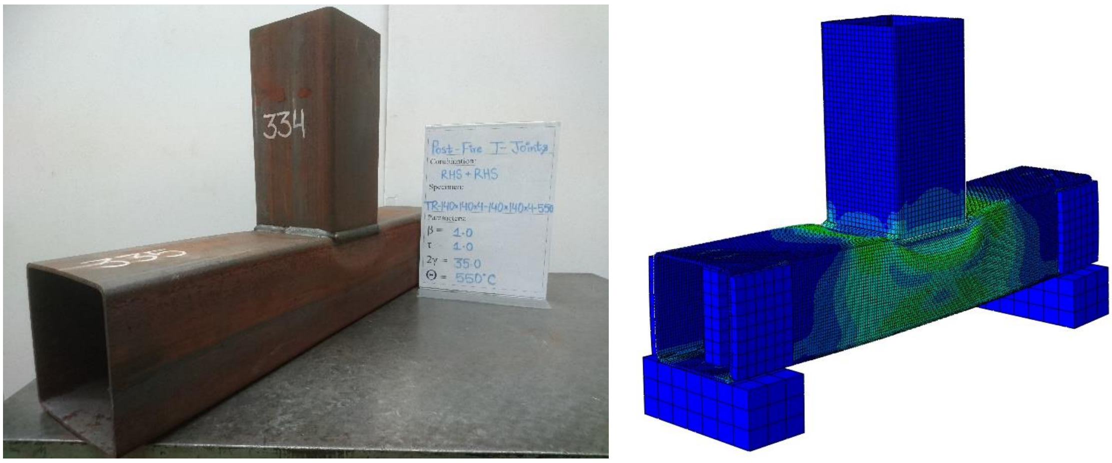

(b) Test vs FE comparison for RHS T-joint with ψ = 550°C and failed by S mode.

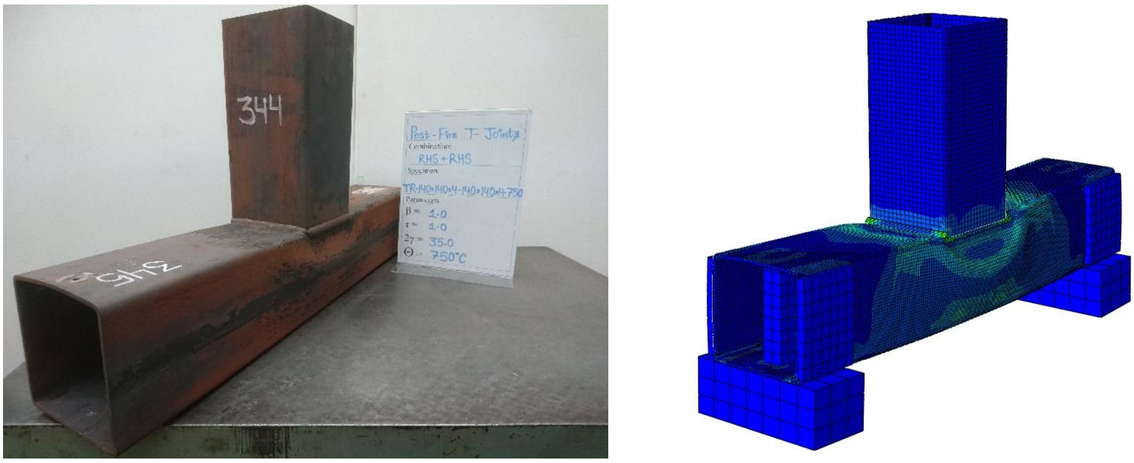

(c) Test vs FE comparison for RHS T-joint with ψ = 750°C and failed by S mode.

Fig. 7. Test vs FE comparisons for RHS T-joints failed by S mode.

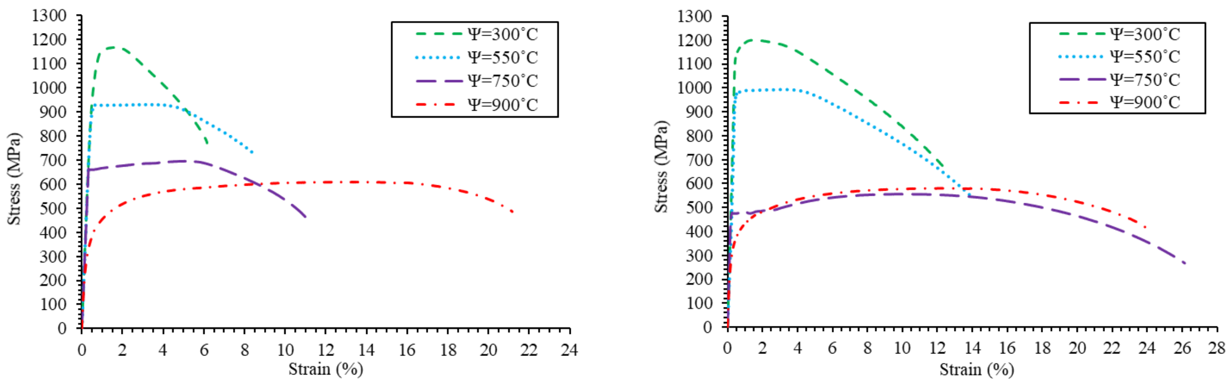

(a) For flat portion.

(b) For corner portion.

Fig. 8. Measured static post-fire stress-strain curves of RHS 120×120×4 [8].

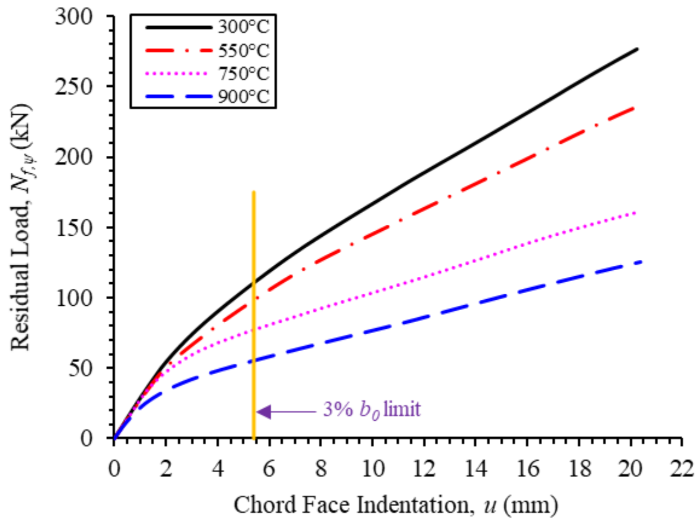

Fig. 9. Variations of load-deformation curves for typical RHS T-joint (T-54×54×4.5-180×100×6; β=0.30) failed by F mode for different fire exposures.

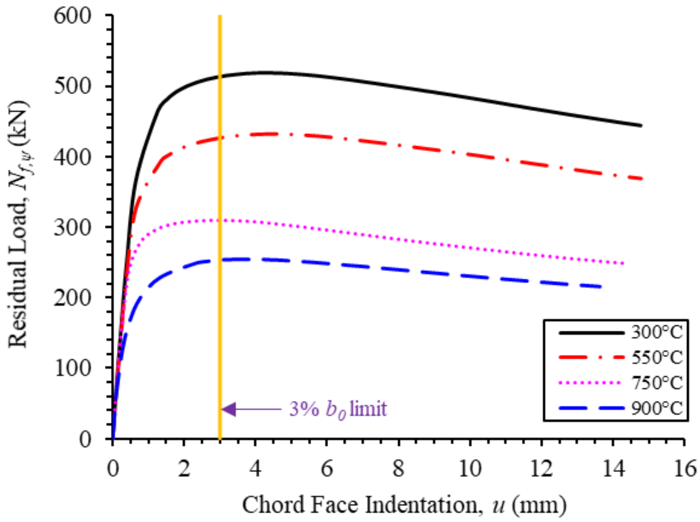

Fig. 10. Variations of load-deformation curves for typical RHS T-joint (T-90×60×6-100×100×6; β=0.90) failed by F+S mode for different fire exposures.

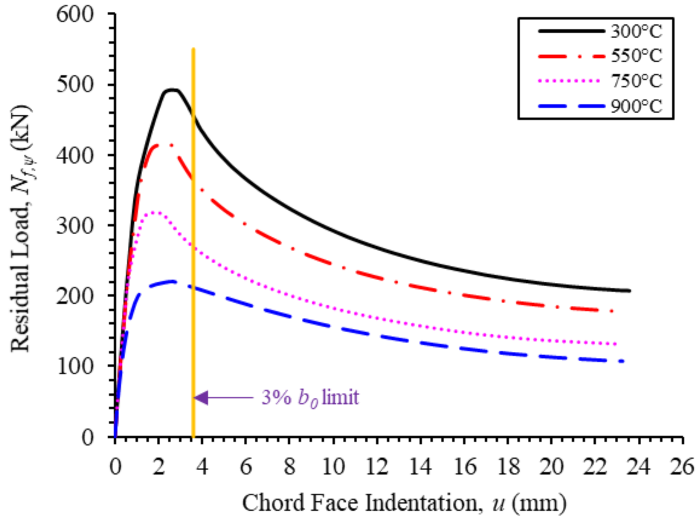

Fig. 11. Variations of load-deformation curves for typical RHS T-joint (T-120×72×4-120×160×4; β=1.0) failed by S mode for different fire exposures.

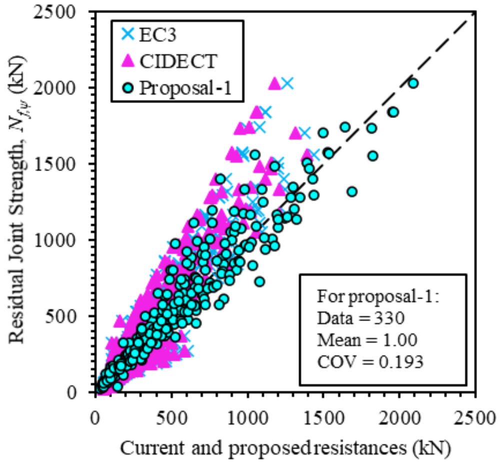

(a) For Proposal-1.

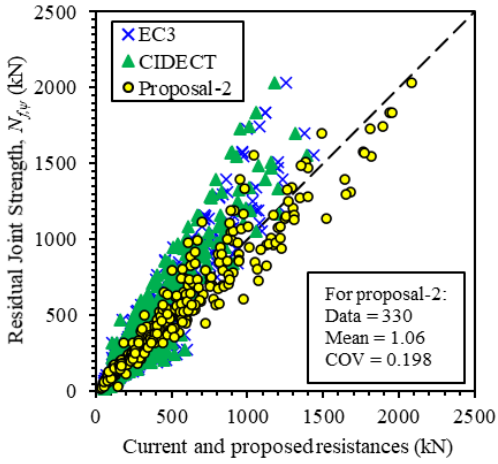

(b) For Proposal-2.

Fig. 12. Comparisons of residual joint strengths with current and proposed nominal resistances for RHS T-joints failed by F mode.

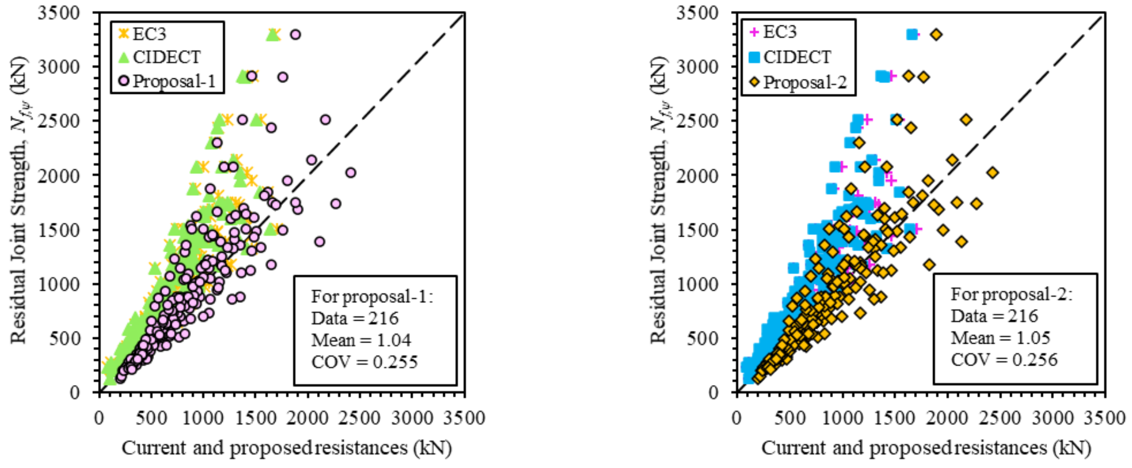

(a) For Proposal-1. (b) For Proposal-2.

Fig. 13. Comparisons of residual joint strengths with current and proposed nominal resistances for RHS T-joints failed by F+S mode.

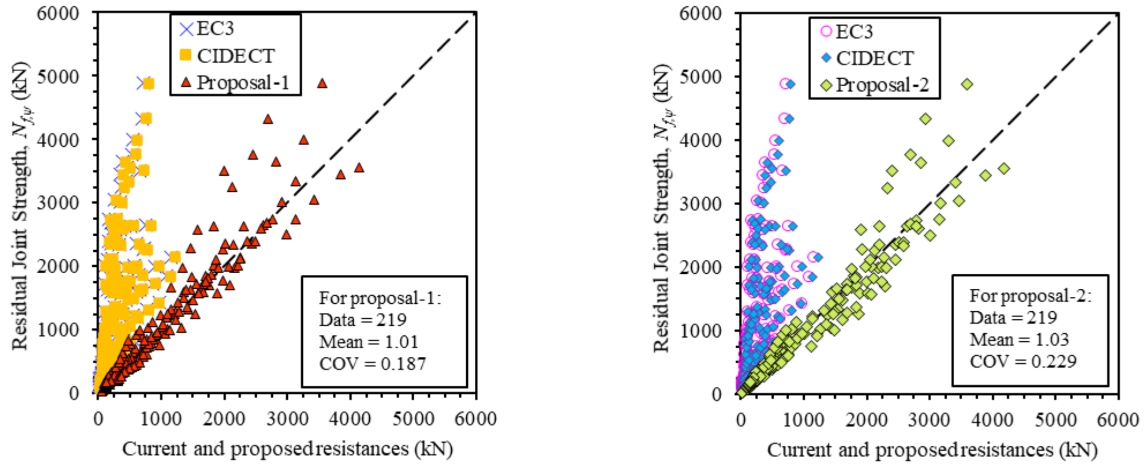

(a) For Proposal-1. (b) For Proposal-2.

Fig. 14. Comparisons of residual joint strengths with current and proposed nominal resistances for RHS T-joints failed by S mode.

Table 1. Measured post-fire mechanical properties [8].

Post-fire Temperatures (˚C)	Sections	Measured mechanical properties							
		Flat region				Corner region			
	(b×h×t)	$E_{f,\Psi}$ (GPa)	$\sigma_{0.2f,\Psi}$ (MPa)	$\sigma_{uf,\Psi}$ (MPa)	$\varepsilon_{ff,\Psi}$ (%)	$E_{c,\Psi}$ (GPa)	$\sigma_{0.2c,\Psi}$ (MPa)	$\sigma_{uc,\Psi}$ (MPa)	$\varepsilon_{fc,\Psi}$ (%)
300	80×80×4	218.2	1144.8	1193.7	6.36	244.1	1196.3	1246.2	11.48
	100×50×4	220.5	1115.5	1120.2	7.29	223.8	1183.9	1201.1	12.76
	120×120×4	221.9	1078.2	1167.5	6.16	237.4	1167.9	1200.0	12.43
	140×140×4	212.3	1087.8	1103.3	7.30	238.7	1117.6	1149.3	11.79
550	80×80×4	214.1	893.7	900.0	8.17	209.4	947.9	951.7	14.12
	100×50×4	209.0	1022.9	1023.1	6.60	240.1	1090.3	1095.4	12.86
	120×120×4	215.7	927.7	930.4	8.43	198.4	983.1	993.1	13.99
	140×140×4	210.8	908.2	911.3	10.00	244.6	950.8	962.7	13.65
750	80×80×4	213.6	729.9	748.5	11.73	216.5	440.3	534.0	25.82
	100×50×4	212.4	780.9	788.8	11.70	230.1	843.8	849.5	14.76
	120×120×4	209.3	659.8	695.2	11.22	238.9	475.6	556.2	26.14
	140×140×4	208.1	653.4	681.7	11.74	219.5	352.4	461.8	29.94
900	80×80×4	202.1	335.1	580.3	24.43	226.0	318.5	551.0	25.31
	100×50×4	204.3	312.9	551.5	25.18	224.0	288.4	497.4	30.35
	120×120×4	201.0	347.4	608.7	21.17	203.0	347.9	580.4	23.90
	140×140×4	197.9	310.0	543.3	23.95	173.3	261.9	470.4	27.91

Table 2. Summary of test vs FE joint strength comparisons for RHS T-joints.

Specimens	Geometric Ratios	Test Strengths[#] (kN)	Numerical Strengths (kN)	
T-b_1×h_1×t_1-b_0×h_0×t_0-Ψ	β	$N_{f,\Psi}$	N_{FE}	$\frac{N_{f,\Psi}}{N_{FE}}$
T-50×100×4-120×120×4-P300˚C	0.41	94.6	94.9	1.00
T-80×80×4-140×140×4-P300˚C	0.57	103.6	106.3	0.97
T-140×140×4-140×140×4-P300˚C	1.00	625.9	623.8	1.00
T-50×100×4-120×120×4-P550˚C	0.42	89.4	90.1	0.99
T-80×80×4-140×140×4-P550˚C	0.57	98.1	97.5	1.01
T-140×140×4-140×140×4-P550˚C	1.00	579.5	572.9	1.01
T-50×100×4-120×120×4-P750˚C	0.41	62.2	62.5	1.00
T-80×80×4-140×140×4-P750˚C	0.57	59.0	58.2	1.01
T-140×140×4-140×140×4-P750˚C	1.00	283.3	281.8	1.01
			Mean	1.00
			COV	0.012

Note: [#]Data obtained from Pandey and Young [1].

Table 3. Summary of comparisons between test and FE residual strengths with existing and proposed nominal resistances for RHS T-joints failed by F mode.

Post-fire Temperatures (ψ)	Parameters	Comparisons $\frac{N_{f,\psi}}{N_{E,\psi}}$	$\frac{N_{f,\psi}}{N_{C,\psi}}$	$\frac{N_{f,\psi}}{N_{pn1}}$	$\frac{N_{f,\psi}}{N_{pn2}}$
300°C	No. of data (n)	83	83	83	83
	Mean (P_m)	1.00	1.20	1.02	1.02
	COV (V_p)	0.289	0.332	0.157	0.156
550°C	No. of data (n)	83	83	83	83
	Mean (P_m)	1.00	1.27	0.98	1.13
	COV (V_p)	0.274	0.313	0.176	0.175
750°C	No. of data (n)	83	83	83	83
	Mean (P_m)	1.04	1.26	0.99	1.09
	COV (V_p)	0.280	0.316	0.207	0.206
900°C	No. of data (n)	81	81	81	81
	Mean (P_m)	1.20	1.39	1.00	1.00
	COV (V_p)	0.308	0.366	0.227	0.227
Overall	No. of data (n)	330	330	330	330
	Mean (P_m)	1.06	1.28	1.00	1.06
	COV (V_p)	0.300	0.337	0.193	0.198
	Resistance factor (ϕ)	1.00	1.00	0.75	0.75
	Reliability index (β_0)	1.36	1.80	2.52	2.67

Table 4. Summary of comparisons between test and FE residual strengths with existing and proposed nominal resistances for RHS T-joints failed by F+S mode.

Post-fire Temperatures (ψ)	Parameters	Comparisons $\frac{N_{f,\psi}}{N_{E,\psi}}$	$\frac{N_{f,\psi}}{N_{C,\psi}}$	$\frac{N_{f,\psi}}{N_{pn1}}$	$\frac{N_{f,\psi}}{N_{pn2}}$
300°C	No. of data (n)	54	54	54	54
	Mean (P_m)	1.15	1.42	1.05	1.01
	COV (V_p)	0.254	0.213	0.250	0.250
550°C	No. of data (n)	54	54	54	54
	Mean (P_m)	1.16	1.47	1.05	1.11
	COV (V_p)	0.240	0.207	0.252	0.252
750°C	No. of data (n)	54	54	54	54
	Mean (P_m)	1.12	1.41	1.07	1.05
	COV (V_p)	0.246	0.205	0.267	0.267
900°C	No. of data (n)	54	54	54	54

	Mean (P_m)	1.35	1.55	0.99	1.00
	COV (V_p)	0.292	0.219	0.247	0.247
Overall	No. of data (n)	216	216	216	216
	Mean (P_m)	1.19	1.46	1.04	1.05
	COV (V_p)	0.271	0.213	0.255	0.256
	Resistance factor (ϕ)	1.00	1.00	0.70	0.70
	Reliability index (β_0)	1.75	2.69	2.53	2.53

Table 5. Summary of comparisons between test and FE residual strengths with existing and proposed nominal resistances for RHS T-joints failed by S mode.

Post-fire Temperatures (ψ)	Parameters	Comparisons			
		$\frac{N_{f,\psi}}{N_{E,\psi}}$	$\frac{N_{f,\psi}}{N_{C,\psi}}$	$\frac{N_{f,\psi}}{N_{pn1}}$	$\frac{N_{f,\psi}}{N_{pn2}}$
300°C	No. of data (n)	55	55	55	55
	Mean (P_m)	5.55	5.93	1.00	0.99
	COV (V_p)	0.771	0.634	0.148	0.150
550°C	No. of data (n)	55	55	55	55
	Mean (P_m)	5.10	5.40	1.02	1.07
	COV (V_p)	0.783	0.595	0.203	0.219
750°C	No. of data (n)	55	55	55	55
	Mean (P_m)	3.99	4.41	1.00	1.07
	COV (V_p)	0.759	0.588	0.203	0.254
900°C	No. of data (n)	54	54	54	54
	Mean (P_m)	2.95	3.59	1.02	0.99
	COV (V_p)	0.629	0.432	0.192	0.263
Overall	No. of data (n)	219	219	219	219
	Mean (P_m)	4.44	4.91	1.01	1.03
	COV (V_p)	0.806	0.624	0.187	0.229
	Resistance factor (ϕ)	1.00	1.00	0.75	0.70
	Reliability index (β_0)	2.31	3.10	2.57	2.63